



Low-temperature plasma-assisted synthesis of iron and nitrogen co-doped CoFeP-N nanowires for high-efficiency electrocatalytic water splitting

Ruiqi Wang^{a,b,1}, Xuxu Sun^{a,b,1}, Junbo Zhong^c, Shengbing Wu^d, Qi Wang^{a,b,c,2,*}, Kostya (Ken) Ostrikov^{e,3}

^a Institute of Plasma Physics, Hefei Institutes of Physical Science, Chinese Academy of Sciences, Hefei 230031, China

^b University of Science and Technology of China, Hefei 230026, China

^c College of Chemical Engineering, Sichuan University of Science and Engineering, Zigong 643000, China

^d Institute of Acupuncture-Moxibustion and Meridians, Anhui Province Key Laboratory of Meridian Viscera Correlation Research Center of Intelligent Equipment Engineering Technology of Traditional Chinese Medicine Rehabilitation and Acupuncture-Moxibustion and Tuina, Anhui Academy of TCM, Hefei 230038, China

^e School of Chemistry and Physics and QUT Centre for Materials Science, Queensland University of Technology (QUT), Brisbane, QLD 4000, Australia

ARTICLE INFO

Keywords:

CoFeP-N nanowires
Co-doping
Plasma nanotechnology
HER
OER
Water splitting

ABSTRACT

Designing efficient, stable, and low-cost non-precious metal electrocatalysts is critical for gainful utilization of renewable resources and effective water splitting. The catalytic efficiency is determined by interactions between the multiple main constituent elements and dopants. However, achieving performance-boosting synergistic interactions between different species in the catalyst is challenging. This work demonstrates such effect using low-temperature plasma-enhanced hydrothermal-phosphorization synthesis of Fe, N co-doped CoFeP-N nanowires. Nickel foam was utilized as the substrate to prepare CoFe-LDH precursor by hydrothermal method and CoFeP nanoparticles were obtained by phosphorization in a tube furnace. The N element was further doped into CoFeP using a low-temperature plasma discharge. The produced CoFeP-N nanowires exhibit far superior hydrogen evolution reaction (HER) and oxygen evolution reaction (OER) activities in an alkaline medium compared to the original CoP due to the incorporation of Fe and N elements, with overpotentials of 64 mV and 219 mV at 10 mA cm⁻² respectively, and excellent cycling stability. When CoFeP-N is used as both the cathode and anode of a two-electrode water splitting device, low voltages of only 1.516 V and 1.636 V were needed to achieve current density of 10 mA cm⁻² and 100 mA cm⁻² respectively, which are better than that of Pt/C||RuO₂ and most non-precious metal-based electrocatalysts reported to date. These experimental results provide new insights and strategies for developing efficient, stable, and low-cost bifunctional water splitting electrocatalysts.

1. Introduction

With the continuous consumption of traditional fossil energy, there is a pressing need to secure new sources of sustainable clean energy to solve the ever-escalating energy and environmental problems [1,2]. Electrocatalytic water splitting for hydrogen and oxygen production, powered by green and sustainable energy systems such as wind energy and tidal energy, is recognized as a promising clean energy production approach [3–5]. The water splitting reaction involves two half-reactions: the hydrogen evolution reaction (HER) at the cathode and the oxygen evolution reaction (OER) at the anode. Currently, the

most widely used materials for HER catalytic activity are Pt noble metals, while Ru/Ir - based materials are commonly used for OER catalytic processes. However, the scarcity and high cost of these metals significantly impede widespread applications of electrocatalysis [6,7]. Therefore, it is of great significance and major challenge to develop efficient, stable, and cheap bifunctional water splitting catalysts.

Recently, Earth-abundant transition metal-based nanomaterials have shown promising prospects as excellent OER/HER electrocatalysts due to their low cost and high catalytic performance. Over the past few years, numerous teams have designed, developed, and evaluated many promising OER/HER catalysts [8–16]. Transition metal phosphide

* Corresponding author at: Institute of Plasma Physics, Hefei Institutes of Physical Science, Chinese Academy of Sciences, Hefei 230031, China.

E-mail address: qiwang@ipp.ac.cn (Q. Wang).

¹ These authors contributed equally to this work

² 0000-0003-3594-2244.

³ 0000-0001-8672-9297.

(TMP) has received strong attention due to its excellent electrocatalytic activity, abundance and low cost; the high activity arises because anions and metal sites act as selective hydride and proton receptors on the TMP surface [4,17–25]. Although great progress has been made, many of the previous TMP catalysts have only shown excellent catalytic effects for one half-reaction while exhibiting poor activity and stability for the other half-reaction, which requires further improvements in the future. Therefore, many attempts have been made to enhance the performance of TMP for the overall water splitting.

Heteroatom doping is a highly effective method for improving the catalytic performance of TMPs. By introducing other elements to generate synergistic effects, the electronic structure of TMP can be optimized, which can be used to adjust the kinetic energy barrier [26]. For example, Ni was doped into FeP-FF and to create a new Ni₂P/FeP heterostructure [27]. This structure achieved a current density of 100 mA cm⁻² at a voltage of only 1.69 V for overall water splitting. Feng et al. synthesized S-doped NiFeP structures derived from MOFs by utilizing S-doped MOFs as precursors via a one-step phosphating process. When the current density of the fully hydrolyzed water reached 10 mA cm⁻², the overpotential was only 1.5 V [28]. Lee et al. developed CoP-nitrogen-doped carbon@NiFeP nanoflakes (CoP-NC@NFP); the overall water splitting device showed the overpotential of 1.57 V at 10 mA cm⁻² [29]. The main components of plasma are free electrons, charged ions, and neutral particles. When plasma discharge occurs, it will ionize the substance into positively charged ions and generate a large number of free electrons. The interaction between high-energy particles in plasma and the material surface can etch the material surface, achieve heteroatom doping, and regulate the electronic arrangement structure. This not only exposes more electrocatalytic active sites, but also enhances the connection between the carrier and the catalyst. The characteristics of high-temperature plasma are almost completely ionized gases and high temperatures of at least 15,000 K, while low-temperature plasma is a partially ionized gas with temperatures typically close to room temperature, making it highly promising for applications. Therefore, low-temperature plasma technology can be an effective strategy for modifying materials [30–33].

Herein, we have successfully prepared bi-functional iron and nitrogen co-doped CoFeP-N nanowires for efficient overall water splitting in alkaline solution using a three-step hydrothermal-phosphating-plasma synthesis method. XPS analysis revealed that the doping of heteroatoms and plasma treatment can effectively enhance the electronic structure of the catalyst, thereby boosting its catalytic ability. Electrochemical HER and OER testing showed that CoFeP-N nanowires presented excellent electrocatalytic activity. In a 1 M KOH aqueous solution, CoFeP-N required only 64 mV and 219 mV to achieve a current density of 10 mA cm⁻², with low Tafel slopes of 80.02 mV dec⁻¹ and 56.08 mV dec⁻¹, respectively, and exhibited excellent cycling stability. Moreover, the water electrolysis system, assembled using the CoFeP-N nanowires as both the cathode and anode, produced a current density of 10 mA cm⁻² at a low voltage of 1.516 V and that of 100 mA cm⁻² at 1.636 V, thus surpassing the commercial Pt/C||RuO₂ electrolytic cell, while also exhibiting superior long-term stability. Overall, this work reports an effective method for preparing transition metal based bifunctional electrocatalysts and creates new avenues for manufacturing efficient, stable, and inexpensive advanced and sustainable energy materials.

2. Experimental details

2.1. Materials and reagents

Cobalt (II) nitrate hexahydrate (Co(NO₃)₂·6 H₂O), iron(III) nitrate nonahydrate (Fe(NO₃)₃·9 H₂O), urea(CO(NH₂)₂), sodium hypophosphite (NaH₂PO₂·H₂O) and potassium hydroxide(KOH) were purchased from Shanghai Aladdin Biochemical Technology Co., Ltd. Ammonium fluoride (NH₄F) was supplied by Sinopharm Chemical

Reagent Co., Ltd. Ruthenium dioxide (RuO₂) was obtained from Shanghai Macklin Biochemical Technology Co., Ltd. Nafion D520 membrane solution (5 wt%) and commercial JM-20% Pt/C were purchased from Shanghai Hesen Electric Co., Ltd., China. Deionized (DI) water was used to prepare solutions. All reagents were used directly without further purification.

2.2. Sample preparation

2.2.1. Synthesis of CoFe-LDH and Co-LDH nanowire array

First, a piece of commercial nickel foam (NF, 2 × 3 cm) was cleaned in 3 M HCl, ethanol, and deionized water by ultrasound for 15 min to remove the surface oxide layer. 1.2 mmol Co(NO₃)₂·6 H₂O, 0.15 mmol Fe(NO₃)₃·9 H₂O, 5 mmol CO(NH₂)₂, and 4 mmol NH₄F were dissolved in 30 mL deionized water while stirring vigorously at room temperature for 1 h to form a well-mixed solution. Then, the mixed solution and foam nickel were transferred into a 50 mL Teflon-lined stainless autoclave, heated at 120°C and kept for 10 h. After slow cooling of the autoclave at room temperature, the CoFe-LDH sample grown on NF was washed with deionized water and dried at 60°C for future use. For comparison, Co-LDH was synthesized using the same methods, except for the absence of Fe(NO₃)₃·9 H₂O.

2.2.2. Synthesis of CoFeP and CoP

In order to synthesize CoFeP and CoP samples, the prepared CoFe-LDH and Co-LDH were placed in the quartz boat at the downstream side of the tube furnace while 1 g NaH₂PO₂·H₂O was placed at the upstream of the tube furnace. Then, the samples were heated at 300°C at the rate of 5°C min⁻¹, and kept at the Ar atmosphere for 2 h, then naturally cooled to ambient temperature.

2.2.3. Synthesis of CoFeP-N and CoP-N

The radio frequency (RF, 13.56 MHz) plasma discharge device is composed of the four main parts: RF power supply, vacuum system, gas source, and discharge chamber. The CoFeP and CoP samples were placed in quartz boats and then introduced into the discharge chamber. The chamber was sealed, and the vacuum pump was activated until the pressure stabilized. H₂ and N₂ gases were used as reaction gases, with the corresponding flow rates set at 15 sccm each. The plasma reaction process takes place at room temperature. The RF power was then turned on, and the power was set to 130 W for a processing time of 15 min. However, the plasma exposure only affects the material's outermost surface. To ensure a more uniform and thorough effect, the samples were removed from the chamber every 5 min, flipped over, and then returned to the quartz boat for further processing. The resulting products were CoFeP-N and CoP-N.

2.3. Characterization

The scanning electron microscopy (SEM) images were obtained using SIRION200 microscope with an electron beam acceleration voltage of 3 kV. The field emission transmission electron microscopy (FETEM) observation was conducted on JEM-2100 F microscope with an electron beam acceleration voltage of 200 kV. The energy dispersive spectroscopy (EDS) mapping and line scanning measurements were conducted on the 200 kV FEI Talos F200X equipped with Super X-EDS system, which includes four windowless silicon drift detectors for fast acquisition. The X-ray diffraction (XRD) patterns were acquired using graphite monochromatized Cu-Kα radiation (λ=1.541178 Å) from 20 to 70°. The X-ray photoelectron spectroscopy (XPS) was conducted on Thermo ESCALAB 250Xi spectrometer with Al Kα=1486.6 eV X-ray source.

2.4. Electrochemical measurements

All electrochemical measurements were conducted at room temperature using a CHI 660E electrochemistry workstation (CH

Instruments, Inc., Shanghai) in a traditional three-electrode configuration. A graphite rod, an Hg/HgO electrode, and the prepared self-supported catalysts (with the approximate geometrical area of 1 cm^2) were used as the counter electrode, reference electrode, and working electrode, respectively. The 1 M KOH aqueous solution was used as the electrolyte. All potentials were calibrated based on a reversible hydrogen electrode (RHE): $E_{\text{RHE}} = E_{\text{Hg/HgO}} + 0.0591 \times \text{pH} + 0.098$. Prior to the HER and OER measurements, the samples were electrochemically activated via cyclic voltammetry (CV) with a scan rate of 50 mV s^{-1} over 40 cycles in the potential range from -0.684 – 0.016 V vs. RHE and from 1.116 to 1.716 V vs. RHE, respectively. The linear sweep voltammetry (LSV) measurements for HER and OER were conducted at scan rates of 5 mV s^{-1} and 1 mV s^{-1} (to minimize the impact of oxidation on OER performance), in the potential range from -0.684 – 0.016 V vs. RHE and from 1.116 to 1.716 V vs. RHE, respectively. All the polarization curves were iR-corrected at the 90% compensated level. Electrochemical impedance spectroscopy (EIS) was performed in the frequency range from 0.01 Hz to 100 kHz at an overpotential of 10 mA cm^{-2} with AC amplitude of 10 mV . The electrochemical double layer capacitance (C_{dl}) for HER and OER was determined by cyclic voltammetry with different scan rates (10 – 100 mV s^{-1}) in the 0.215 – 0.315 V range vs. RHE and 0.66 – 0.76 V vs. RHE, respectively. The electrochemical active surface area (ECSA) can be calculated based on equation $\text{ECSA} = C_{\text{dl}}/C_s$, where C_s is the specific capacitance and is assumed to be a constant. It is generally reported that C_s for ordinary flat surface is generally between 0.022 and 0.130 mF cm^{-2} . For the estimates of surface area, general specific capacitances of $C_s = 0.040 \text{ mF cm}^{-2}$ based on typical reported values [34], so the ECSA is calculated using the following formula :

$$\text{ECSA} = C_{\text{dl}} / 0.040 \text{ mF cm}^{-2}$$

where C_{dl} is the double layer capacitance of the catalyst. The chronopotentiometry analysis was carried out under a current density of 10 mA cm^{-2} .

2.5. Theoretical calculations

The density functional theory (DFT) calculations were carried out with the VASP code [35]. The Perdew–Burke–Ernzerhof (PBE) functional within the generalized gradient approximation (GGA) [36] was used to process the exchange–correlation interactions, while the projector-augmented-wave pseudopotential (PAW) [37] was applied with a kinetic energy cut-off of 500 eV , which was utilized to describe the expansion of the electronic eigenfunctions. The vacuum layer thickness was set to be 25 \AA to minimize the interlayer interactions. The Brillouin-zone integration was sampled by a Γ -centered $5 \times 5 \times 1$ Monkhorst–Pack k-point. All atomic positions were fully relaxed until

the energy and force reached a tolerance of $1 \times 10^{-5} \text{ eV}$ and 0.03 eV/\AA , respectively. The dispersion corrected DFT-D method was employed to consider the long-range interactions [38].

The Gibbs free energy change (ΔG) was calculated by computational hydrogen electrode (CHE) model as follows:

$$\Delta G = \Delta E + \Delta \text{ZPE} - T\Delta S$$

where ΔE is the reaction energy obtained by the total energy difference between the reactant and product molecules absorbed on the catalyst surface and ΔS is the change in entropy for each reaction, ΔZPE is the zero-point energy correction to the Gibbs free energy. Here, T represents room temperature (298.15 K).

3. Result and discussion

3.1. Synthesis and characterizations of catalysts

Fig. 1 shows a brief overview of the synthesis process involved in preparing CoFeP-N catalysts, which includes the following three steps: (1) utilizing $\text{Co}(\text{NO}_3)_2 \cdot 6 \text{ H}_2\text{O}$, $\text{Fe}(\text{NO}_3)_3 \cdot 9 \text{ H}_2\text{O}$, $\text{Co}(\text{NH}_2)_2$, and NH_4F as raw materials, using NF as a carrier to prepare CoFe-LDH by hydrothermal method, (2) using $\text{NaH}_2\text{PO}_2 \cdot \text{H}_2\text{O}$ as the phosphorus source, preparing CoFeP through phosphorization in a tube furnace, (3) incorporating N element into CoFeP using RF plasma discharge under H_2 and N_2 atmosphere to develop CoFeP-N nanowires.

Figure S2 shows the Scanning Electron Microscope (SEM) images of different catalysts, showcasing the distinct morphological characteristics resulting from different processing methods. Notably, CoP displays a simple coral-like structure consisting of rough nanowire arrays, while CoP-N forms clusters of nanowires with small surface branches. CoFeP displays a rough surface array of nanosheets, whereas CoFeP-N features a sleek surface cluster of nanowires. These different modifications impart unique morphological characteristics to the catalysts, which subsequently influence their catalytic performance. Transmission Electron Microscopy (TEM) images in Fig. 2a corroborate that CoFeP-N has a needle-like nanowire structure. Additionally, the High-Resolution Transmission Electron Microscopy (HRTEM) image in Fig. 2b indicates that cobalt phosphide in the red box as the main body with the doping material appearing in the form of iron phosphide in the green box. Moreover, the clear lattice stripes with crystal plane spacing of 0.314 nm and 0.183 nm shown in Fig. 2c correspond to the (211) crystal plane of CoP_3 and the (112) crystal plane of FeP_2 , respectively. Elemental mapping images and X-ray Energy Dispersive Spectroscopy (EDS) data of different elements in CoFeP-N are displayed in Figs. 2d and S3. These images highlight the uniform distribution of Co, Fe, P, and N elements on CoFeP-N nanowires, with higher concentration of Co and P as the

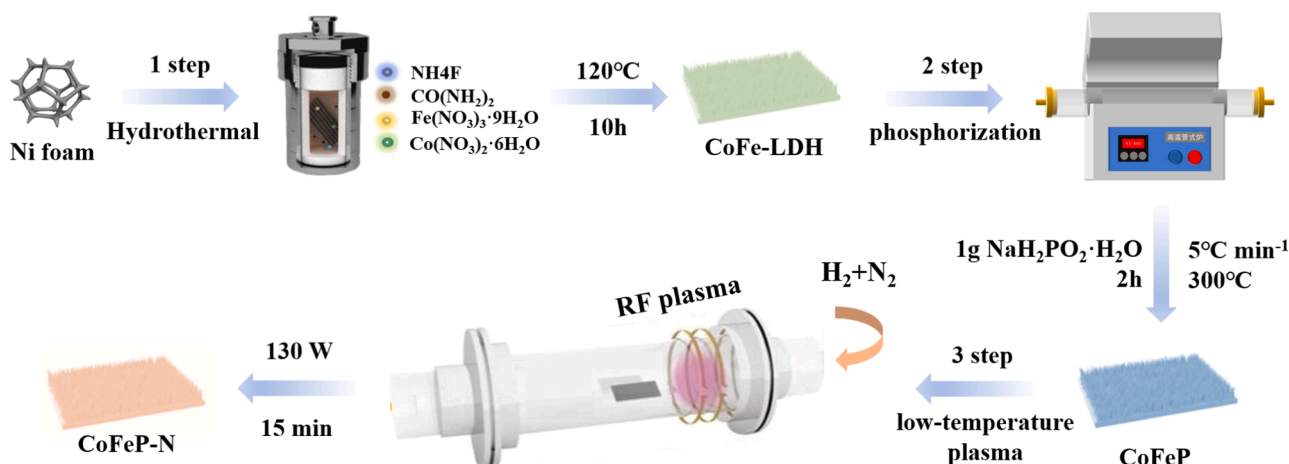


Fig. 1. Preparation process of CoFeP-N catalyst.

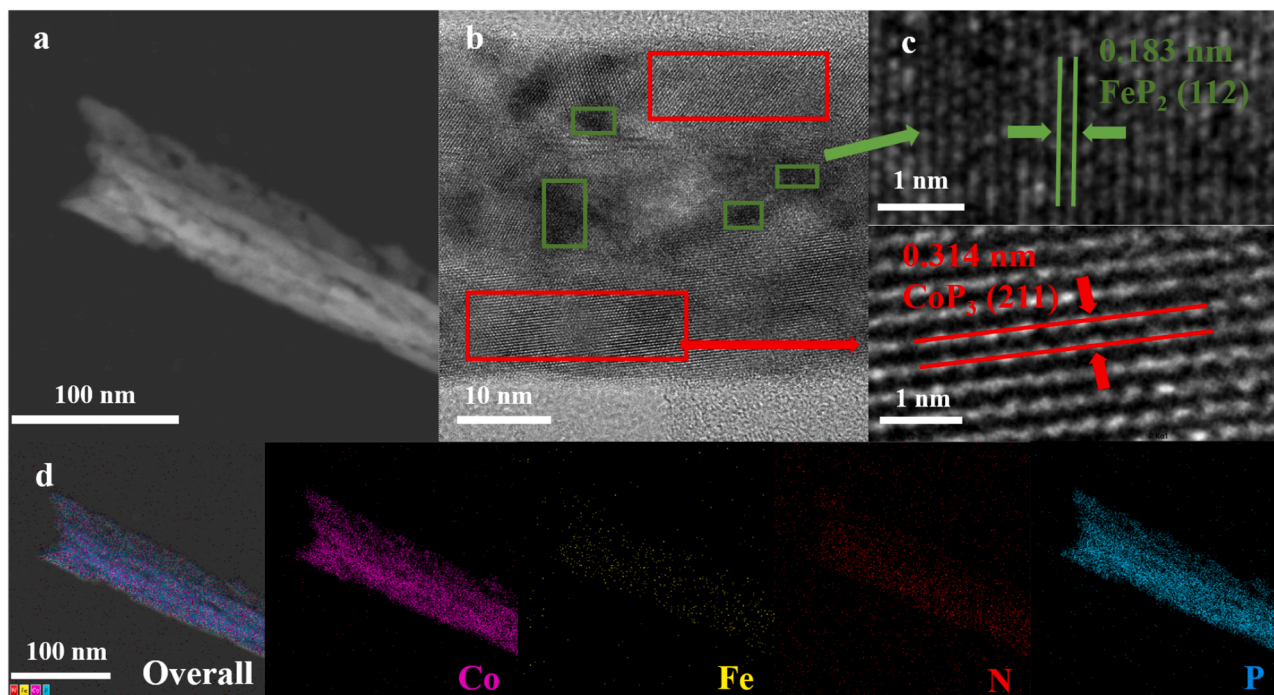


Fig. 2. (a) TEM images and (b, c) HRTEM images of CoFeP-N. (d) Overall elemental mapping, distribution of Co, Fe, N, and P elements in CoFeP-N nanowires.

main body and lower concentration of Fe and N as the doping material. Finally, TEM and HRTEM images of pure CoP, CoP-N, and CoFeP are presented in Figure S4, thereby allowing a clear view of the typical

lattice stripes of cobalt phosphide and iron phosphide.

The crystal structures of four different catalysts were analyzed using X-ray diffraction (XRD) patterns. As shown in Figure S5, the peaks of

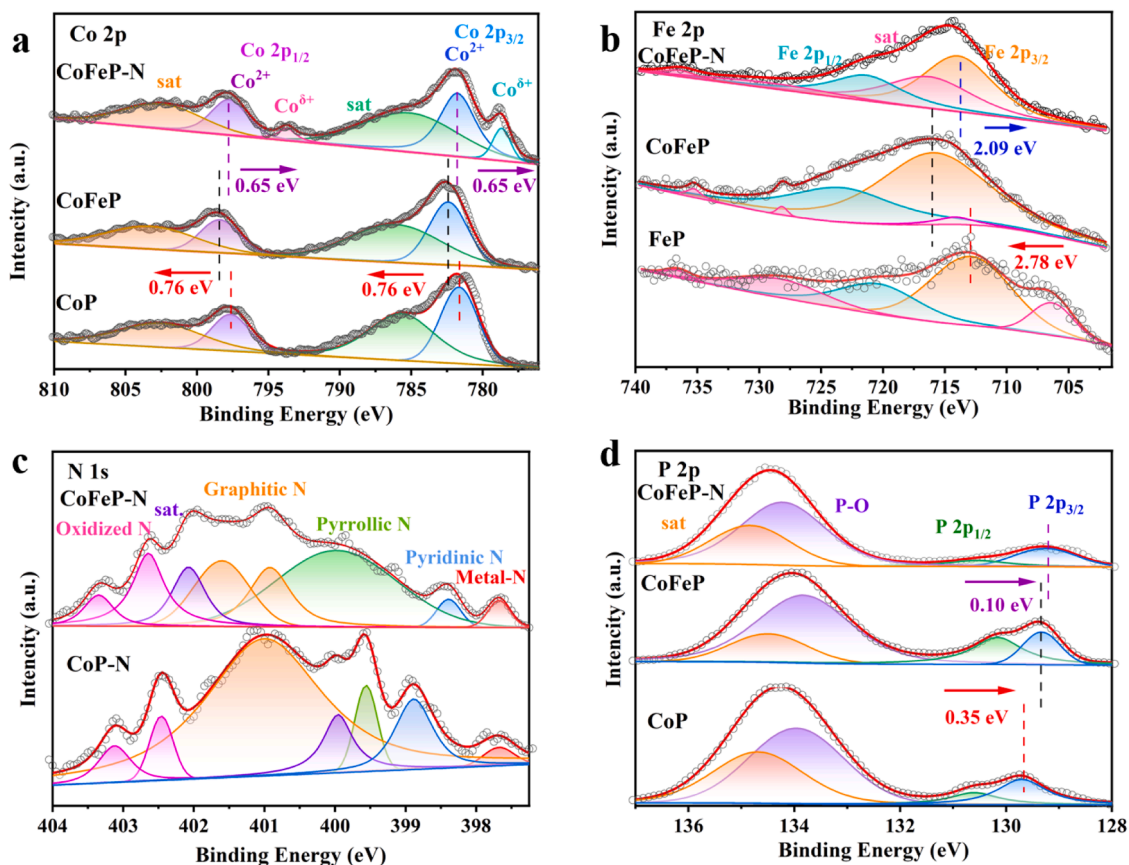


Fig. 3. (a) Co 2p spectra of CoFeP-N and CoFeP and CoP. (b) Fe 2p spectra of CoFeP-N, CoFeP and FeP. (c) N 1s spectra of CoFeP-N and CoP-N. (d) P 2p spectra of CoFeP-N and CoFeP and CoP.

CoFeP-N at 36.64° , 41.03° , 47.39° , and 56.63° correspond to the (013), (222), (400), and (332) planes in the CoP_3 standard card (JCPDS PDF # 73-1239), respectively. The peaks at 31.72° and 48.46° correspond to the (013) and (222) planes in the FeP_2 standard card (JCPDS PDF # 06-0561). The two clear peaks at 44.83° and 55.22° can be attributed to the nickel foam substrate. The surface electronic valence states and chemical composition of different catalysts were further analyzed using X-ray photoelectron spectroscopy (XPS). Figure S6a shows that the surface of CoFeP-N contains Co, Fe, P, N, C, and O elements. Element C originates from the nickel foam substrate, while element O can be attributed to inevitable oxidation caused by the catalyst surface exposed to air. Two peaks with the binding energy (BE) of 781.7 eV and 797.7 eV on the Co 2p XPS spectrum of CoFeP-N correspond to the Co^{2+} 2p_{3/2} and Co^{2+} 2p_{1/2} produced by Co-P. Co^{6+} 2p_{3/2} and 2p_{1/2} signals can be observed at the BE peak positions of 778.7 eV and 793.7 eV [23]. The other two peaks are the satellite peaks of 785.1 eV and 802.4 eV [23, 39]. Similarly, in the Fe 2p spectrum of CoFeP-N shown in Fig. 3b, the two peaks at 713.57 eV and 721.07 eV correspond to the Fe 2p_{3/2} and Fe 2p_{1/2} produced by Fe-P. The peak with the BE of 715.93 eV, 728.93 eV, 736.35 eV is the satellite peak [20]. From Fig. 3c, metal-N (metal=Co, Fe) at 397.65 eV, pyridine N at 398.4 eV, pyrrole N at 400.05 eV, graphite N at 400.9 eV and 401.9 eV, oxidized N at 402.65 eV and 403.35 eV can be distinguished from the N 1s spectrum of CoFeP-N [4]. Fig. 3d shows that the peaks at 129.25 eV and 130.55 eV correspond to the BE of P 2p_{3/2} and P 2p_{1/2} of CoFeP-N, respectively, which are attributed to the phosphorus anion of metal phosphide [19]. The main peak at 134.2 eV is due to oxidation or oxygen doping in the air during

phosphating [40,41]. Compared with CoP, the Co 2p_{3/2} and Co 2p_{1/2} orbitals of CoFeP shifted forward by 0.76 eV, indicating that Co experienced electron loss. Meanwhile, the P 2p_{3/2} and 2p_{1/2} orbitals of CoFeP shifted negatively by 0.35 eV compared to CoP, indicating that P received electrons. It can be seen that the introduction of Fe can change the electron configuration of the original CoP and can effectively improve the electrocatalytic activity. In addition, compared to CoFeP, the Co 2p_{3/2} and 2p_{1/2} orbitals of CoFeP-N shifted negatively by 0.65 eV, the Fe 2p_{3/2} and 2p_{1/2} orbitals shifted negatively by 2.09 eV, and the P 2p_{3/2} and 2p_{1/2} orbitals shifted negatively by 0.10 eV. This finding indicates that after the N plasma treatment, many free electrons generated by the plasma discharge are captured by the material, allowing Co, Fe, and P to acquire electrons. In addition, due to the reduction effect of H₂ plasma, a portion of Co^{2+} in CoFeP-N is reduced to $\text{Co}^{\delta+}$. This rearrangement of atomic charges can effectively improve the electrocatalytic activity [11,42]. Furthermore, the XPS spectra of Co 2p and P 2p of CoP-N are shown in Figure S6c, d. To investigate the surface charge transfer at the interface between CoP₂ and FeP₂, XPS testing was conducted on P 2p of FeP₂ as well. Figure S7 shows that the peaks of P 2p_{3/2} and P 2p_{1/2} in CoFeP exhibit a positive shift in comparison to pure FeP, while they display a negative shift when compared to pure CoP. This change in binding energy suggests that the strong interaction at the interface between CoP₂ and FeP₂ in CoFeP results in charge redistribution, which can greatly enhance the electrocatalytic activity [42].

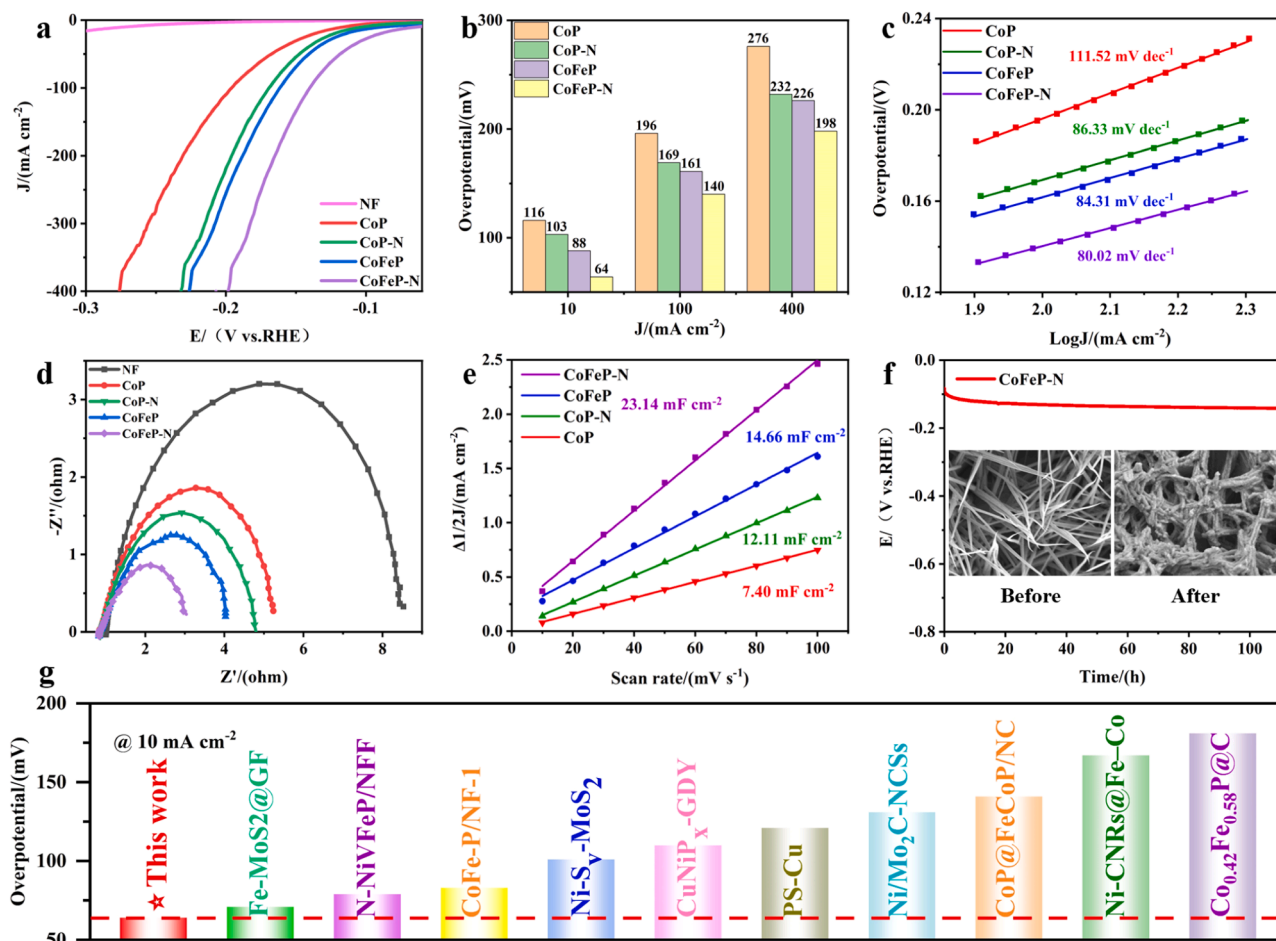


Fig. 4. (a) HER polarization curve, (b) overpotential, (c) Tafel curve, (d) Nyquist plot, (e) electric double layer capacitance of different materials. (f) The potential versus time curve at a current density of 10 mA cm^{-2} and the SEM images of the catalyst before and after testing of CoFeP-N. (g) Comparison of HER overpotential with the recently reported electrocatalysts from Table S3.

3.2. Electrocatalytic performance of catalysts for HER and OER

First, the HER performance of CoFeP-N nanowire arrays was investigated using a conventional three-electrode system in a 1 M KOH solution. As a control, we also tested CoP, CoP-N, and CoFeP with the same loading capacity. Fig. 4a shows the LSV curves of the various catalysts. CoFeP-N nanowires exhibited the best HER catalytic activity compared to CoP, CoP-N, and CoFeP. Fig. 4b shows that at a current density of 10 mA/cm^2 , the overpotential of CoFeP-N is only 64 mV, which is significantly better than those of CoP (116 mV), CoP-N (103 mV), and CoFeP (88 mV). To gain further insights into the catalytic mechanisms, we conducted a series of tests. Firstly, we calculated the Tafel slopes of different catalysts, as shown in Fig. 4c. It can be observed that CoFeP-N has the smallest Tafel slope ($80.02 \text{ mV dec}^{-1}$), which is lower than CoP ($111.52 \text{ mV dec}^{-1}$), CoP-N ($86.33 \text{ mV dec}^{-1}$), CoFeP ($84.31 \text{ mV dec}^{-1}$), indicating that CoFeP-N has more advantages in reaction kinetics [19]. From the electrochemical impedance spectra (EIS) in Fig. 4d, it can be seen that the charge transfer resistance (R_{ct}) of CoFeP-N is significantly lower than that of other materials, which means a high electron transfer rate and dynamic process [43]. As shown in Figs. 4e, S8 and Table S1, we measured the electrochemical double-layer capacitances (C_{dl}) of various catalysts by cyclic voltammetry at different scanning rates in the unladen region and estimated the electrochemical surface areas (ECSA) of different catalysts accordingly. It is evident that CoFeP-N has the largest

C_{dl} (23.14 mF cm^{-2}), far exceeding that of CoP (7.40 mF cm^{-2}), CoP-N (12.11 mF cm^{-2}), and CoFeP (14.66 mF cm^{-2}), which also leads to its largest ECSA (578.5 cm^2), indicating that it has more active sites required for the reaction [44]. The LSV curve normalized by ECSA shown in Figure S9 shows the optimal HER activity of CoFeP-N compared to other catalysts. Moreover, in addition to catalytic activity, CoFeP-N exhibits excellent stability, as shown in Figs. 4f and S10. After continuous operation for 100 h at a current density of 10 mA cm^{-2} , there was only a slight decrease in the potential. The SEM comparison of electrode materials before and after cyclic stability testing shows that after 100 h of HER, the original nanowire structure collapsed, which may be the reason for the decrease in the potential.

We further investigated the effect of the plasma on catalytic materials. We treated CoFeP catalysts for different durations and at varying discharge powers. The results shown in Figure S11 indicate that with an increase in the discharge power and treatment time, the HER catalytic performance of the catalysts initially increases and then decreases. We selected a discharge power of 130 W and a treatment time of 15 min as the optimal conditions for the plasma treatment of CoFeP materials. These conditions were chosen because at low discharge power and short processing time, the effect of the plasma on the material is not clear. On the other hand, under the high discharge power or prolonged processing time, the high energy of the plasma species may cause significant damage to the material. To the best of our knowledge, the HER

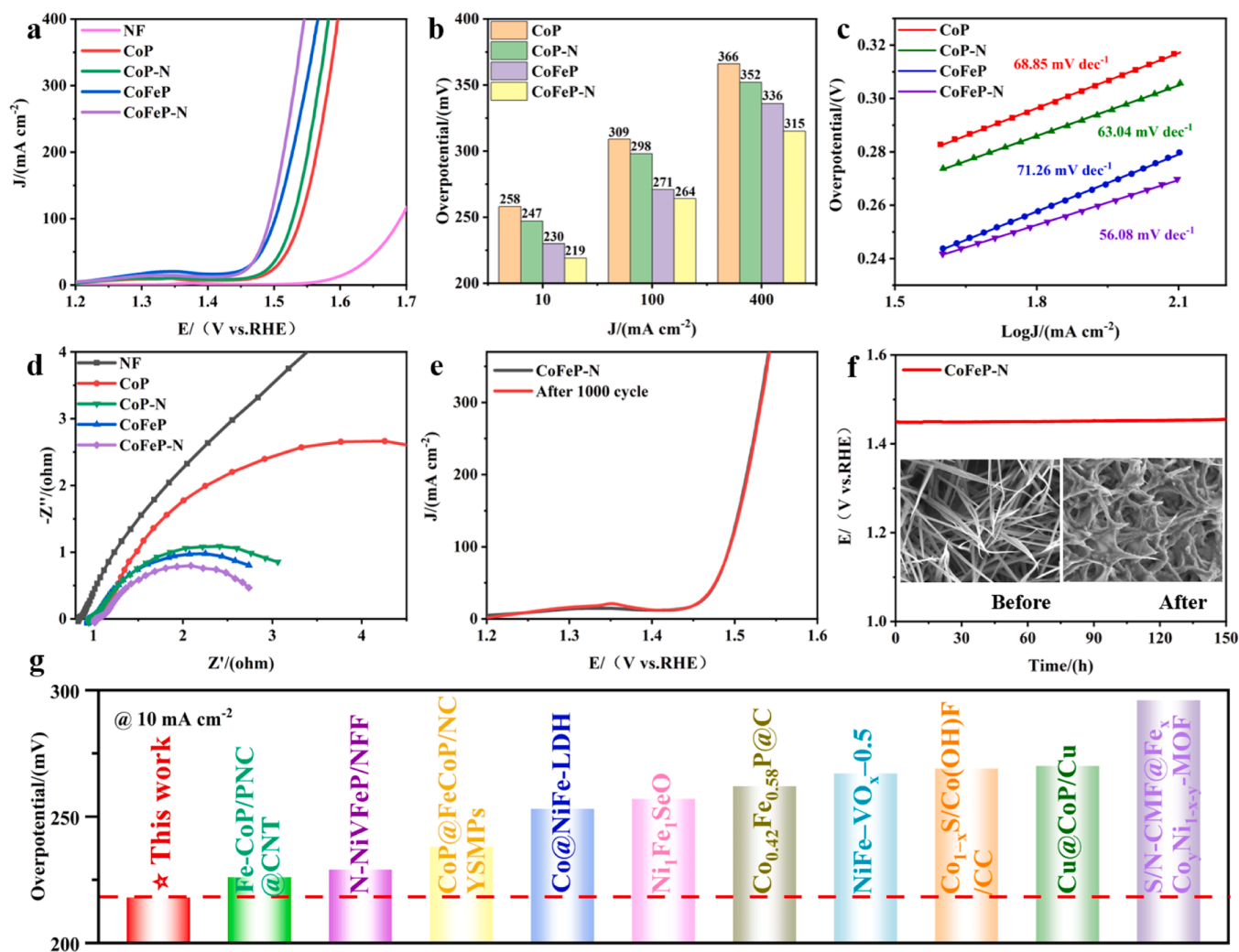


Fig. 5. (a) OER polarization curve, (b) overpotential, (c) Tafel curve, (d) Nyquist plot of different materials. (e) The OER polarization curve of CoFeP-N after testing 1000 CVs. (f) The potential versus time curve at a current density of 10 mA cm^{-2} and the SEM images of the catalyst before and after testing of CoFeP-N. (g) Comparison of OER overpotential with the recently reported electrocatalysts from Table S4.

overpotential in this work is lower than many other recently reported electrocatalysts as shown in Fig. 4g.

In addition to HER, the OER performances of different catalysts were also tested under the same experimental conditions. From the LSV curve in Fig. 5a, it can be seen that CoFeP-N catalyst shows the best OER activity. Since oxidation peaks appear when measuring in OER LSV, backward measurements were added in Figure S12 to describe the overpotentials at 10 mA cm⁻². Fig. 5b more specifically indicates that the overpotentials of CoFeP-N at 10 mA cm⁻², 100 mA cm⁻², and 400 mA cm⁻² are 219 mV, 264 mV, and 315 mV, respectively, which are much lower than those of CoP (258 mV, 309 mV, and 366 mV), CoP-N (247 mV, 298 mV, and 352 mV), and CoFeP (230 mV, 271 mV, and 336 mV). As shown in Fig. 5c, CoFeP-N has the smallest Tafel slope (56.08 mV dec⁻¹), which is lower than CoP (68.85 mV dec⁻¹), CoP-N (63.04 mV dec⁻¹), and CoFeP (71.26 mV dec⁻¹), indicating that it boosts the reaction kinetics. The EIS in Fig. 5d shows that CoFeP-N exhibits the lowest R_{ct} , indicating a higher charge transfer rate during the catalytic process. In addition, as shown in Figures S13, S14, and Table S2, the C_{dl} of CoFeP-N is greater than that of CoP, CoP-N, and CoFeP, with the highest ECSA. The LSV curve normalized by ECSA shown in Figure S15 still shows the optimal OER activity of CoFeP-N in these catalysts. Surprisingly, Fig. 5e and f show that CoFeP-N has excellent OER stability, with almost negligible differences before and after 1000 CV cycles. After continuous operation for 150 h at a current density of 10 mA cm⁻², the potential only changed by 7 mV. Fig. 5f shows the SEM comparison of electrode materials before and after the cyclic stability testing. One can see that after 150 h of HER, although the original nanowire structure has some slight changes, needle-like structures that are similar to the original structure can still be seen. This finding, indicates that CoFeP-N can still maintain good morphological and structural stability before and after the OER reaction while maintaining the high efficiency of the catalytic reaction. Similarly, as shown in Figure S16, we treated CoFeP catalysts for 10, 15, 20, and 25 min at discharge powers of 100, 130, and 150 W, respectively, and investigated the effect of the plasma treatment on the OER catalytic activity. As before, a discharge power of 130 W and a processing time of 15 min showed the best improvement effect on the OER performance of the material. The OER overpotential in this work is lower compared to the many other recently reported electrocatalysts as shown in Fig. 4g.

In addition, the XRD and XPS spectra of Co 2p, Fe 2p are also shown in Figure S17 and S18 for CoFeP-N electrocatalyst after HER and OER chronopotentiometry testing. Before and after the reaction, the XRD patterns demonstrated insignificant changes, indicating that the catalysts has the stable crystal. From the XPS spectrum, it is evident that both the Co 2p and Fe 2p orbitals have undergone changes after the completion of HER and OER reactions. However, the magnitude of change observed in OER is smaller compared to HER. This suggests that the catalyst's electronic structure remains more stable during the OER reaction, which could explain why the cyclic stability of the catalyst is superior in OER compared to HER.

From Figs. 4 and 5, one can see that the HER and OER catalytic performance of iron and nitrogen co-doped CoFeP-N nanowires are superior to the vast majority of the reported non noble metal based electrocatalysts. Its excellent electrochemical catalytic performance may be attributed to the following factors: (i) The flower-like shaped nanowires of CoFeP-N expose more reaction areas in the electrolytic medium, and the largest ECSA of CoFeP-N indicates that it has more active sites, which is conducive to the transmission and diffusion of electrons and ions in the HER and OER processes. (ii) The doping of iron atoms can induce a synergistic effect with cobalt atoms, which will change the electronic structure of the electrocatalyst and enhance its intrinsic activity, leading to the HER and OER activities that are superior to those of single metal phosphide. The plasma treatment introduced nitrogen to improve the conductivity of the catalyst, and provided additional electrons to iron atoms, thus increasing the electron transfer rate of the electrode. In addition, the heterogeneous interface formed between

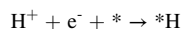
CoP₃ and FeP₂ can serve as the active reaction center, playing an important role in improving the performance of HER and OER. In summary, these factors explain the excellent catalytic performance of iron and nitrogen co-doped CoFeP-N nanowires for electrocatalytic hydrogen and oxygen evolution reactions.

3.3. Water splitting performance of CoFeP-N

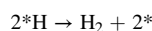
Due to the excellent HER and OER performance of CoFeP-N, a dual electrode electrolytic cell was assembled by employing the CoFeP-N as both anode and cathode simultaneously to test the material's overall water splitting performance in alkaline media and to explore its potential as a bifunctional electrocatalyst. For comparison, Pt/C and RuO₂ catalysts supported on nickel foam were used as cathode and anode, respectively, to build the electrolytic cell. Similarly, LSV by backward measurement was used to describe the overpotentials at 10 mA cm⁻² because of the oxidation peak. As shown in Figs. 6a, b, e, S19 and Table S5, the current density of CoFeP-N||CoFeP-N electrolytic cell can reach 10 mA cm⁻², 100 mA cm⁻², and 400 mA cm⁻² at a low voltage of 1.516 V, 1.636 V and 1.810 V, which is better than 1.549 V, 1.736 V and 1.868 V of Pt/C||RuO₂ electrolytic cell. This result is also better than for most of the reported non noble metal based electrocatalysts. In addition, the results of the time-voltage test show that the CoFeP-N||CoFeP-N electrolytic cell has excellent cycle stability, and can work continuously for more than 100 h at a current density of 100 mA cm⁻² without any significant potential variation.

4. Reaction mechanisms revealed by theoretical calculations

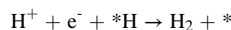
To elucidate the potential mechanisms of the significantly enhanced HER and OER activity, theoretical studies were conducted on CoP, CoFeP, and CoFeP-N electrocatalysts using DFT calculations. Figure S20 displays the atomic models and band structures of CoP, CoFeP, and CoFeP-N that were used for the theoretical calculations. The HER reaction process typically involves the adsorption of protons on the catalytic site surface through the Volmer reaction,



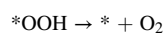
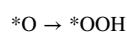
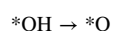
and the desorption of H₂ through the Tafel



or Heyrovsky



reactions, where * represents the active site in the catalyst. Regardless of the specific adsorption or desorption processes followed, the catalytic activity of HER and the Gibbs free energy (ΔG_{*H}) of hydrogen bonds is closely related. The closer the ΔG_{*H} is to the theoretical value of 0 eV, the stronger the adsorption and desorption activity of *H [45]. Fig. 7a displays the ΔG_{*H} value of CoP, CoFeP and CoFeP-N in terms of HER. It can be observed that, compared to CoFeP-N with a ΔG_{*H} of -0.14 eV, CoP (-0.42 eV) and CoFeP (-0.26 eV) are further away from 0 eV. This finding suggests that the introduction of Fe and N atoms can enhance the adsorption and desorption of *H, ultimately significantly improving the HER activity. OER in alkaline solutions typically follows the four electron oxidation processes [2]:



Based on the above reaction processes, the Gibbs free energies of CoP, CoFeP, and CoFeP-N in the three intermediates of OER were further

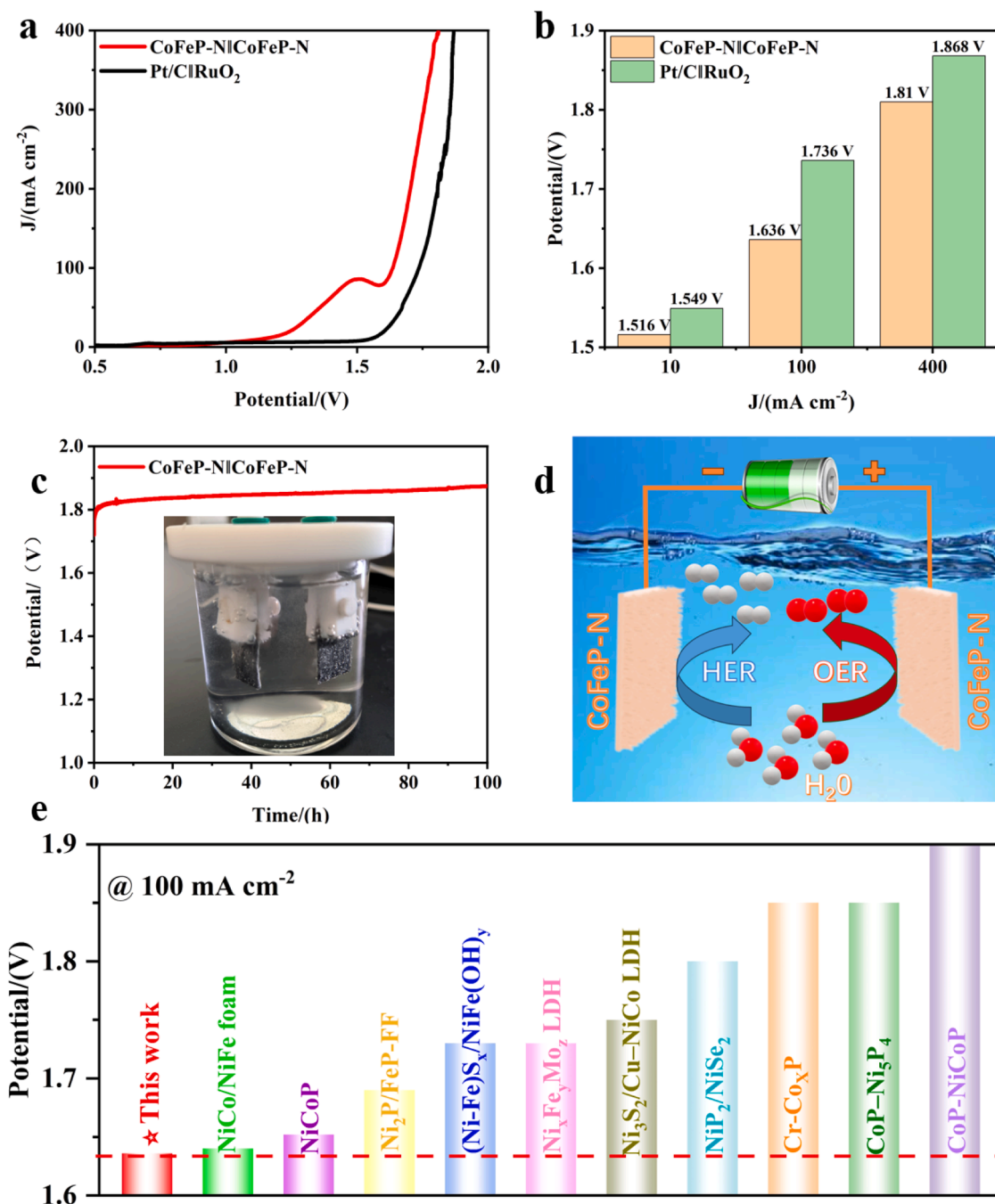


Fig. 6. (a) Water splitting polarization curve and (b) potential at 10 mA cm⁻², 100 mA cm⁻² and 400 mA cm⁻² of CoFeP-N|CoFeP-N and Pt/C|RuO₂. (c) Cyclic stability test at 100 mA cm⁻² of CoFeP-N. (d) Schematic of CoFeP-N|CoFeP-N used as the anode and cathode for overall water splitting. (e) Comparison of water splitting potential with the recently reported electrocatalysts from Table S5.

calculated, as shown in Fig. 7b. Table S6 presents the calculated free energy differences of three catalysts in different reaction processes in the step-by-step catalytic reaction. It can be seen from Table S6 that for CoP, the reaction process $\ast\text{O} \rightarrow \ast\text{OOH}$ has the highest reaction energy barrier, which can be regarded as the rate determining step (RDS) of the catalytic material in the OER reaction. Similarly, the reaction process $\ast\text{OOH} \rightarrow \ast + \text{O}_2$ can be considered as the RDS of CoFeP and CoFeP-N. Among them, the RDS energy barrier of CoFeP-N is 2.02 eV, which is lower than 2.26 eV of CoP and 2.19 eV of CoFeP, indicating that CoFeP-N can catalyze OER reactions faster and achieve better OER performance. At the same time, the density of states (DOS) of CoP, CoFeP, and CoFeP-N were calculated to analyze the changes in the electronic structure of the catalyst. As shown in Fig. 7c, it is evident that the DOS of CoFeP-N near

the Fermi level (EF) is higher than that of CoFeP and is much higher than that of CoP. This finding indicates that CoFeP-N has a narrower bandgap, which can reduce the energy barrier for the electron transfer and has a better electron transfer ability [46]. This effect appears because the introduction of iron atoms significantly increases the probability of electron distribution at the Fermi level, and the doping of nitrogen atoms also provides additional electrons, which is beneficial for improving the conductivity of the material [47]. Differential charge density can be used to describe the state of electron accumulation and depletion more accurately. From Fig. 7d, one can see that the electron accumulation and consumption of CoFeP-N catalyst mainly occur near the N atom, indicating that the introduction of N element can promote electron transfer and change the charge distribution [48] within the

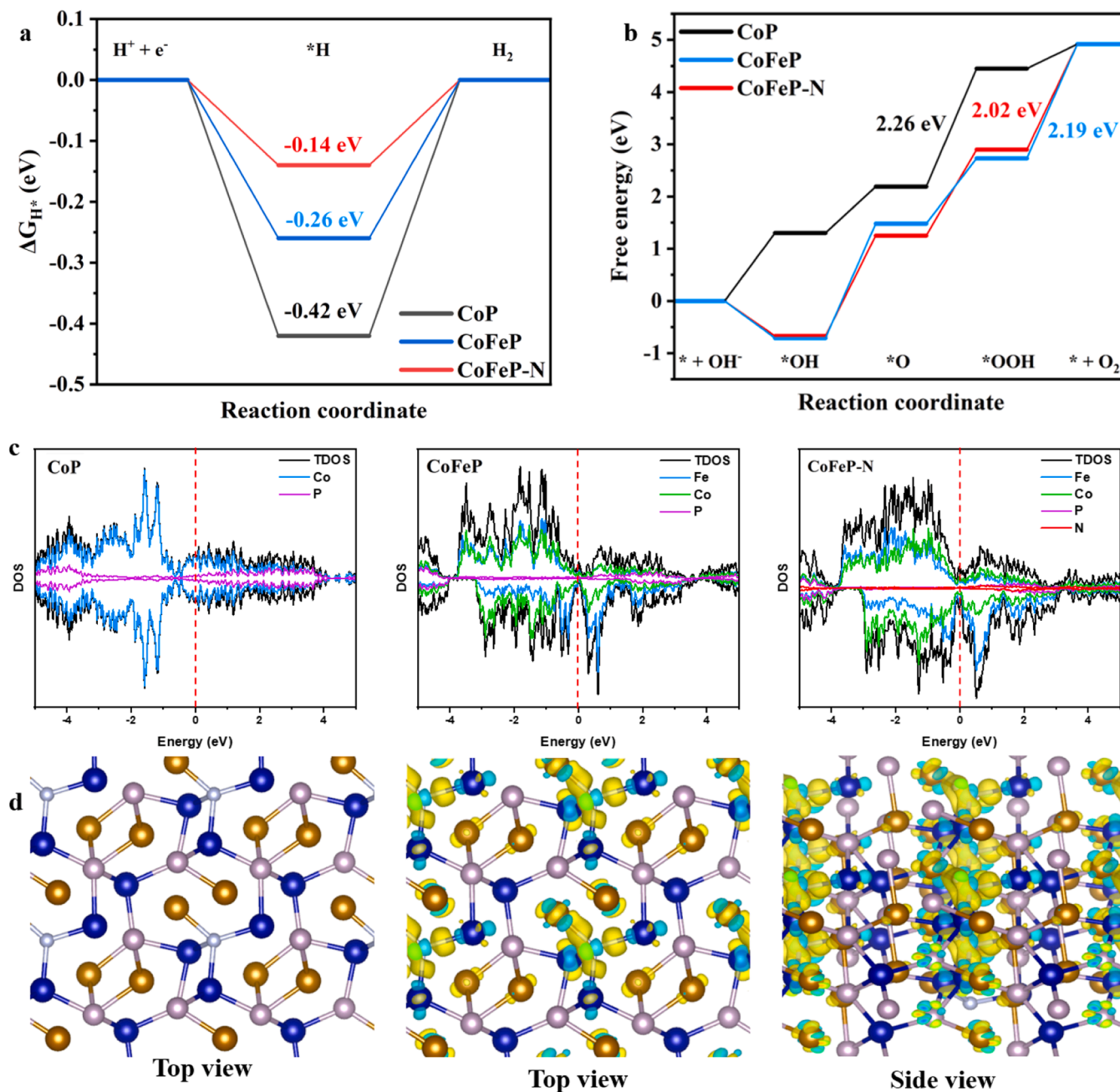


Fig. 7. The Gibbs free energy diagram of the intermediate steps toward (a) HER and (b) OER. (c) The density of states of CoP, CoFeP and CoFeP-N. (d) The schematic of charge density difference of CoFeP-N, yellow and blue regions respectively manifest the charge accumulation and depletion.

material. The accumulation of abundant electrons can promote the occurrence of HER reactions, and the accumulation of holes in transition metal phosphides induced by the electron transfer can in turn be used to adsorb OER intermediates, thereby accelerating the HER and OER reactions [48,49].

In summary, CoFeP-N exhibits superior HER and OER activity, primarily due to the introduction of iron, which enhances the active surface and interface sites of the catalytic material. Additionally, the nitrogen element provides additional electrons, resulting in a more conductive electronic structure for the CoFeP-N catalyst material compared to CoFeP. Consequently, electron transfer within the catalyst material is accelerated. The findings from DFT calculations align well with the electrochemical experimental data, further confirming that iron and nitrogen co-doped CoFeP-N nanowires are very promising catalysts for water electrolysis.

5. Conclusion

Designing efficient, stable, and low-cost non-precious metal electrocatalysts is critical for gainful utilization of renewable resources and effective water splitting. The catalytic efficiency is determined by interactions between the multiple main constituent elements and dopants. However, achieving performance-boosting synergistic interactions between different species in the catalyst is challenging.

To address these issues, a dual functional CoFeP-N nanowires for hydrogen and oxygen evolution have been successfully prepared through a versatile synthesis method involving the hydrothermal, phosphating, and low-temperature plasma processing steps. The catalytic tests of HER and OER have demonstrated that CoFeP-N shows high electrocatalytic activity and good cyclic stability. This effect can be attributed to its rich reactive active site, the synergistic effect between

Co/Fe and the treatment and modification by N₂ plasmas. In addition, the double electrode electrolysis of the water system assembled by CoFeP-N||CoFeP-N can provide a current density of 100 mA cm⁻² at only 1.636 V, which is far superior to Pt/C||RuO₂ electrolytic cell, and it also shows excellent long-term stability. This work provides an effective approach to develop efficient, stable, and inexpensive bifunctional transition metal catalysts for overall water splitting.

CRediT authorship contribution statement

Qi Wang: Writing – review & editing, Validation, Supervision, Project administration, Funding acquisition. **Shengbing Wu:** Resources. **Junbo Zhong:** Resources. **Xuxu Sun:** Writing – review & editing, Writing – original draft, Methodology, Investigation, Formal analysis, Data curation, Conceptualization. **Ruiqi Wang:** Writing – review & editing, Writing – original draft, Methodology, Investigation, Formal analysis, Data curation, Conceptualization. **Kostya (Ken) Ostrikov:** Writing – review & editing, Supervision, Conceptualization.

Declaration of Competing Interest

The authors declare that they have no known competing financial interests or personal relationships that could have appeared to influence the work reported in this paper.

Data availability

Data will be made available on request.

Acknowledgements

This research was financially supported by the National Key R&D Program of China (2022YFC3500500, 2022YFC3500502), the Anhui Provincial Natural Science Foundation (No. 2208085MA16), the Anhui Provincial Key Research and Development Plan (No. 1704a0902017), the Anhui Provincial Natural Science Foundation for Distinguished Young Scholars of China (No. 1608085J03), K. O. acknowledges partial support from the Australian Research Council (ARC) and QUT Centre for Materials Science.

Appendix A. Supporting information

Supplementary data associated with this article can be found in the online version at doi:10.1016/j.apcatb.2024.124027.

References

- [1] Y. Luo, Z. Zhang, M. Chhowalla, B. Liu, Recent advances in design of electrocatalysts for high-current-density water splitting, *Adv. Mater.* 34 (2022) 2108133, <https://doi.org/10.1002/adma.202108133>.
- [2] Z.Y. Yu, Y. Duan, X.Y. Feng, X. Yu, M.R. Gao, S.H. Yu, Clean and affordable hydrogen fuel from alkaline water splitting: past, recent progress, and future prospects, *Adv. Mater.* 33 (2021) 2007100, <https://doi.org/10.1002/adma.202007100>.
- [3] P. Balasubramanian, S.-B. He, A. Jansirani, H.-H. Deng, H.-P. Peng, X.-H. Xia, W. Chen, Engineering of oxygen vacancies regulated core-shell N-doped carbon@NiFe₂O₄ nanospheres: a superior bifunctional electrocatalyst for boosting the kinetics of oxygen and hydrogen evolution reactions, *Chem. Eng. J.* 405 (2021) 126732, <https://doi.org/10.1016/j.cej.2020.126732>.
- [4] J. Shi, F. Qiu, W. Yuan, M. Guo, Z.-H. Lu, Nitrogen-doped carbon-decorated yolk-shell CoP@FeCoP micro-polyhedra derived from MOF for efficient overall water splitting, *Chem. Eng. J.* 403 (2021) 126312, <https://doi.org/10.1016/j.cej.2020.126312>.
- [5] K. Chen, X.-L. Wang, W. Hu, Q. Kong, H. Pang, Q. Xu, Modified metal–organic frameworks for electrochemical applications, *Small Struct.* 3 (2022) 2100200, <https://doi.org/10.1002/sstr.202100200>.
- [6] S. Marini, P. Salvi, P. Nelli, R. Pesenti, M. Villa, M. Berrettoni, G. Zangari, Y. Kiros, Advanced alkaline water electrolysis, *Electrochim. Acta* 82 (2012) 384–391, <https://doi.org/10.1016/j.electacta.2012.05.011>.
- [7] P. Zhu, X. Xiong, D. Wang, Regulations of active moiety in single atom catalysts for electrochemical hydrogen evolution reaction, *Nano Res* 15 (2022) 5792–5815, <https://doi.org/10.1007/s12274-022-4265-y>.
- [8] Y. Jia, L. Zhang, G. Gao, H. Chen, B. Wang, J. Zhou, M.T. Soo, M. Hong, X. Yan, G. Qian, J. Zou, A. Du, X. Yao, A Heterostructure coupling of exfoliated Ni-Fe hydroxide nanosheet and defective graphene as a bifunctional electrocatalyst for overall water splitting, *Adv. Mater.* 29 (2017) 1700017, <https://doi.org/10.1002/adma.201700017>.
- [9] L. Zhang, Y. Jia, G. Gao, X. Yan, N. Chen, J. Chen, M.T. Soo, B. Wood, D. Yang, A. Du, X. Yao, Graphene defects trap atomic ni species for hydrogen and oxygen evolution reactions, *Chem* 4 (2018) 285–297, <https://doi.org/10.1016/j.chempr.2017.12.005>.
- [10] Q. Che, Q. Li, Y. Tan, X. Chen, X. Xu, Y. Chen, One-step controllable synthesis of amorphous (Ni-Fe)S /NiFe(OH) hollow microtube/sphere films as superior bifunctional electrocatalysts for quasi-industrial water splitting at large-current-density, *Appl. Catal. B Environ.* 246 (2019) 337–348, <https://doi.org/10.1016/j.apcatb.2019.01.082>.
- [11] S. Liu, R. Wan, Z. Lin, Z. Liu, Y. Liu, Y. Tian, D.-D. Qin, Z. Tang, Probing the Co role in promoting the OER and Zn–air battery performance of NiFe-LDH: a combined experimental and theoretical study, *J. Mater. Chem. A* 10 (2022) 5244–5254, <https://doi.org/10.1039/d1ta11055a>.
- [12] B. Wu, S. Gong, Y. Lin, T. Li, A. Chen, M. Zhao, Q. Zhang, L. Chen, A unique NiOOH@FeOOH heteroarchitecture for enhanced oxygen evolution in saline water, *Adv. Mater.* 34 (2022) e2108619, <https://doi.org/10.1002/adma.202108619>.
- [13] Y. Ma, D. Leng, X. Zhang, J. Fu, C. Pi, Y. Zheng, B. Gao, X. Li, N. Li, P.K. Chu, Y. Luo, K. Huo, Enhanced activities in alkaline hydrogen and oxygen evolution reactions on MoS₂ electrocatalysts by in-plane sulfur defects coupled with transition metal doping, *Small* 18 (2022) 2203173, <https://doi.org/10.1002/smll.202203173>.
- [14] Y. Zhao, X.F. Lu, Z.P. Wu, Z. Pei, D. Luan, X.W.D. Lou, Supporting trimetallic metal-organic frameworks on s/n-doped carbon macroporous fibers for highly efficient electrocatalytic oxygen evolution, *Adv. Mater.* 35 (2023) 2207888, <https://doi.org/10.1002/adma.202207888>.
- [15] H. Shi, Y. Zhang, N. Pang, S. Xu, D. Xiong, L. Wang, P. Yang, P.K. Chu, Surface conductance analysis of X-MoS₂ (X = Fe, Co, Ni) prepared on graphite felt as bifunctional catalysts for the hydrogen/oxidation evolution reactions, *Electrochim. Acta* 439 (2023) 141596, <https://doi.org/10.1016/j.electacta.2022.141596>.
- [16] E. Enkhtuvshin, S. Yeo, H. Choi, K.M. Kim, B.S. An, S. Biswas, Y. Lee, A.K. Nayak, J. U. Jang, K.H. Na, W.Y. Choi, G. Ali, K.H. Chae, M. Akbar, K.Y. Chung, K. Yoo, Y. C. Chung, T.H. Shin, H. Kim, C.Y. Chung, H. Han, Surface reconstruction of ni-fe layered double hydroxide inducing chloride ion blocking materials for outstanding overall seawater splitting, *Adv. Funct. Mater.* 33 (2023) 2214069, <https://doi.org/10.1002/adfm.202214069>.
- [17] H. Fan, W. Chen, G. Chen, J. Huang, C. Song, Y. Du, C. Li, K. Ostrikov, Plasma-heteroatom-doped Ni-V-Fe trimetallic phospho-nitride as high-performance bifunctional electrocatalyst, *Appl. Catal. B Environ.* 268 (2020) 118440, <https://doi.org/10.1016/j.apcatb.2019.118440>.
- [18] J. Li, S. Zou, X. Liu, Y. Lu, D. Dong, Electronically modulated CoP by Ce doping as a highly efficient electrocatalyst for water splitting, *ACS Sustain. Chem. Eng.* 8 (2020) 10009–10016, <https://doi.org/10.1021/acssuschemeng.0c01193>.
- [19] Y. Deng, Y. Cao, Y. Xia, X. Xi, Y. Wang, W. Jiang, D. Yang, A. Dong, T. Li, Self-templated synthesis of CoFeP @ C cage-in-cage superlattices for enhanced electrocatalytic water splitting, *Adv. Energy Mater.* 12 (2022) 2202394, <https://doi.org/10.1002/aenm.202202394>.
- [20] M. Guo, Y. Yuan, Y. Qu, T. Yu, C. Yuan, Z.H. Lu, Porous N-doped carbon with confined Fe-doped CoP grown on CNTs for superefficient oxygen evolution electrocatalysis, *Chem. Commun.* 58 (2022) 1597–1600, <https://doi.org/10.1039/d1cc06923c>.
- [21] J. Gao, Y. Li, X. Yu, Y. Ma, Graphdiyne reinforced multifunctional Cu/Ni bimetallic Phosphides-Graphdiyne hybrid nanostructure as high performance electrocatalyst for water splitting, *J. Colloid Interface Sci.* 628 (2022) 508–518, <https://doi.org/10.1016/j.jcis.2022.07.150>.
- [22] K. Zhang, W. Ma, G. Tan, Z. Cheng, Y. Ma, W. Li, X. Feng, Z. Li, Interfacial engineering of Ru-doped Co₃O₄/CoP nanowires heterostructure as efficient bifunctional electrocatalysts for alkaline water splitting, *Mol. Catal.* 530 (2022) 112640, <https://doi.org/10.1016/j.mcat.2022.112640>.
- [23] D. Xu, Z. Kang, H. Zhao, Y. Ji, W. Yao, D. Ye, J. Zhang, Coupling heterostructured CoP-NiCoP nanopin arrays with MXene (Ti₃C₂T_x) as an efficient bifunctional electrocatalyst for overall water splitting, *J. Colloid Interface Sci.* 639 (2023) 223–232, <https://doi.org/10.1016/j.jcis.2023.02.052>.
- [24] J. Jiang, G. Xu, Y. Li, C. Wang, L. Zhang, Interfacial engineering of metal–organic framework derived hierarchical CoP–Ni₅P₄ nanosheet arrays for overall water splitting, *J. Mater. Chem. A* 11 (2023) 1801–1809, <https://doi.org/10.1039/d2ta06866d>.
- [25] Z. Liu, T. Zhang, Y. Lin, H. Jia, Y. Wang, Y. Wang, G. Zhang, Highly N-doped Fe/Co phosphide superstructures for efficient water splitting, *Small* (2023) 2302475, <https://doi.org/10.1002/smll.202302475>.
- [26] H. Zhang, A.W. Maijenburg, X. Li, S.L. Schweizer, R.B. Wehrspohn, Bifunctional heterostructured transition metal phosphides for efficient electrochemical water splitting, *Adv. Funct. Mater.* 30 (2020) 2003261, <https://doi.org/10.1002/adfm.202003261>.
- [27] M. Jiang, H. Zhai, L. Chen, L. Mei, P. Tan, K. Yang, J. Pan, Unraveling the synergistic mechanism of bi-functional nickel–iron phosphides catalysts for overall water splitting, *Adv. Funct. Mater.* 33 (2023) 2302621, <https://doi.org/10.1002/adfm.202302621>.
- [28] S. Li, L. Wang, H. Su, A.N. Hong, Y. Wang, H. Yang, L. Ge, W. Song, J. Liu, T. Ma, X. Bu, P. Feng, Electron redistributed s-doped nickel iron phosphides derived from one-step phosphatization of MOFs for significantly boosting electrochemical water

- splitting, *Adv. Funct. Mater.* 32 (2022) 2200733, <https://doi.org/10.1002/adfm.202200733>.
- [29] E. Vijayakumar, S. Ramakrishnan, C. Sathiskumar, D.J. Yoo, J. Balamurugan, H. S. Noh, D. Kwon, Y.H. Kim, H. Lee, MOF-derived CoP-nitrogen-doped carbon@NiFeP nanoflakes as an efficient and durable electrocatalyst with multiple catalytically active sites for OER, HER, ORR and rechargeable zinc-air batteries, *Chem. Eng. J.* 428 (2022) 131115, <https://doi.org/10.1016/j.cej.2021.131115>.
- [30] D. Wang, Y. Zou, L. Tao, Y. Zhang, Z. Liu, S. Du, S. Zang, S. Wang, Low-temperature plasma technology for electrocatalysis, *Chin. Chem. Lett.* 30 (2019) 826–838, <https://doi.org/10.1016/j.cclet.2019.03.051>.
- [31] Q. Jiang, H. Zhang, S. Wang, Plasma-enhanced low-temperature solid-state synthesis of spinel LiMn_2O_4 with superior performance for lithium-ion batteries, *Green. Chem.* 18 (2016) 662–666, <https://doi.org/10.1039/c5gc01563d>.
- [32] K. Xu, H. Cheng, H. Lv, J. Wang, L. Liu, S. Liu, X. Wu, W. Chu, C. Wu, Y. Xie, Controllable surface reorganization engineering on cobalt phosphide nanowire arrays for efficient alkaline hydrogen evolution reaction, *Adv. Mater.* 30 (2018), <https://doi.org/10.1002/adma.201703322>.
- [33] P. Yan, T. Yang, M. Lin, Y. Guo, Z. Qi, Q. Luo, X.Y. Yu, “One stone five birds” plasma activation strategy synergistic with Ru single atoms doping boosting the hydrogen evolution performance of metal hydroxide, *Adv. Funct. Mater.* 33 (2023), <https://doi.org/10.1002/adfm.202301343>.
- [34] C.C. McCrory, S. Jung, J.C. Peters, T.F. Jaramillo, Benchmarking heterogeneous electrocatalysts for the oxygen evolution reaction, *J. Am. Chem. Soc.* 135 (2013) 16977–16987, <https://doi.org/10.1021/ja407115p>.
- [35] J.F.G. Kresse, Efficiency of ab-initio total energy calculations for metals and semiconductors using a plane-wave basis set, *Comp. Mater. Sci.* 6 (1996) 15–50, [https://doi.org/10.1016/0927-0256\(96\)00008-0](https://doi.org/10.1016/0927-0256(96)00008-0).
- [36] K.B. John P. Perdew, Matthias Ernzerhof, Generalized gradient approximation made simple, *Phys. Rev. Lett.* 77 (1996) 3865–3868, <https://doi.org/10.1103/PhysRevLett.77.3865>.
- [37] P.E. Blochl, Projector augmented-wave method, *Phys. Rev. B* 50 (1994) 17953–17979, <https://doi.org/10.1103/physrevb.50.17953>.
- [38] S. Grimme, Semiempirical GGA-type density functional constructed with a long-range dispersion correction, *J. Comput. Chem.* 27 (2006) 1787–1799, <https://doi.org/10.1002/jcc.20495>.
- [39] C. Guan, W. Xiao, H. Wu, X. Liu, W. Zang, H. Zhang, J. Ding, Y.P. Feng, S. J. Pennycook, J. Wang, Hollow Mo-doped CoP nanoarrays for efficient overall water splitting, *Nano Energy* 48 (2018) 73–80, <https://doi.org/10.1016/j.nanoen.2018.03.034>.
- [40] F. Luo, Q. Zhang, X. Yu, S. Xiao, Y. Ling, H. Hu, L. Guo, Z. Yang, L. Huang, W. Cai, H. Cheng, Palladium phosphide as a stable and efficient electrocatalyst for overall water splitting, *Angew. Chem. Int. Ed.* 57 (2018) 14862–14867, <https://doi.org/10.1002/anie.201810102>.
- [41] D. Chen, H. Bai, J. Zhu, C. Wu, H. Zhao, D. Wu, J. Jiao, P. Ji, S. Mu, Multiscale hierarchical structured nicop enabling ampere-level water splitting for multi-scenarios green energy-to-hydrogen systems, *Adv. Energy Mater.* 13 (2023) 2300499, <https://doi.org/10.1002/aenm.202300499>.
- [42] X. Huang, X. Xu, X. Luan, D. Cheng, CoP nanowires coupled with CoMoP nanosheets as a highly efficient cooperative catalyst for hydrogen evolution reaction, *Nano Energy* 68 (2020) 104332, <https://doi.org/10.1016/j.nanoen.2019.104332>.
- [43] W.J. Kang, Y. Feng, Z. Li, W.Q. Yang, C.Q. Cheng, Z.Z. Shi, P.F. Yin, G.R. Shen, J. Yang, C.K. Dong, H. Liu, F.X. Ye, X.W. Du, Strain-activated Copper Catalyst for pH-universal hydrogen evolution reaction, *Adv. Funct. Mater.* 32 (2022) 2112367, <https://doi.org/10.1002/adfm.202112367>.
- [44] K. Wang, S. Wang, K.S. Hui, H. Gao, D.A. Dinh, C. Yuan, C. Zha, Z. Shao, Z. Tang, K. N. Hui, Synergistically boosting the elementary reactions over multiheterogeneous ordered macroporous $\text{Mo}_2\text{C}/\text{NC}$ -Ru for highly efficient alkaline hydrogen evolution, *Carbon Energy* 4 (2022) 856–866, <https://doi.org/10.1002/cey2.188>.
- [45] D. Chen, Z. Pu, P. Wang, R. Lu, W. Zeng, D. Wu, Y. Yao, J. Zhu, J. Yu, P. Ji, S. Mu, Mapping hydrogen evolution activity trends of intermetallic Pt-group silicides, *ACS Catal.* 12 (2022) 2623–2631, <https://doi.org/10.1021/acscatal.1c05175>.
- [46] X. Ji, Y. Lin, J. Zeng, Z. Ren, Z. Lin, Y. Mu, Y. Qiu, J. Yu, Graphene/ MoS_2 /FeCoNi (OH)_x and Graphene/ MoS_2 /FeCoNiP_x multilayer-stacked vertical nanosheets on carbon fibers for highly efficient overall water splitting, *Nat. Commun.* 12 (2021) 1380, <https://doi.org/10.1038/s41467-021-21742-y>.
- [47] D.I. Jeong, H.W. Choi, S. Woo, J.H. Yoo, D. Kang, S. Kim, B. Lim, J.H. Kim, S.-W. Kim, B.K. Kang, D.H. Yoon, Electronic structure modification and N-doped carbon shell nanoarchitectonics of $\text{Ni}_3\text{FeN}/\text{NC}$ for overall water splitting performance evaluation, *J. Mater. Chem. A* 10 (2022) 16704–16713, <https://doi.org/10.1039/d2ta04817e>.
- [48] A. Kumar, S. Bhattacharyya, Porous NiFe-oxide nanocubes as bifunctional electrocatalysts for efficient water-splitting, *ACS Appl. Mater. Inter.* 9 (2017) 41906–41915, <https://doi.org/10.1021/acsaami.7b14096>.
- [49] Y. Gu, S. Chen, J. Ren, Y.A. Jia, C. Chen, S. Komarneni, D. Yang, X. Yao, Electronic structure tuning in $\text{Ni}_3\text{FeN}/\text{r-GO}$ aerogel toward bifunctional electrocatalyst for overall water splitting, *ACS Nano* 12 (2018) 245–253, <https://doi.org/10.1021/acsnano.7b05971>.